Available online at www.sciencedirect.com

ScienceDirect

Advances in Space Research 72 (2023) 2786–2800

ADVANCES IN SPACE RESEARCH (a COSPAR publication)

www.elsevier.com/locate/asr

Space debris remediation using space-based lasers

Lewis Walker, Massimiliano Vasile *

University of Strathclyde, Glasgow G1 1XJ, United Kingdom

Received 30 June 2022; received in revised form 15 June 2023; accepted 19 June 2023
Available online 23 June 2023

Abstract

Centimetre and sub-centimetre debris fragments present a significant threat to many operational satellites in Earth orbit. When debris can be tracked, the preferred approach is collision avoidance to slightly alter the orbit of the at-risk satellite, resulting in an along-track displacement which compounds over several orbits. Although numerous strategies for active debris removal and remediation have been proposed, most such methods involve rendezvous maneuvers with targeted pieces of debris prior to some mechanical interaction. While such approaches are appropriate for removing larger objects which are potential sources of further debris, they are unsuitable for application to fragments which are too small to be accurately tracked from Earth and with which a rendezvous would be challenging.

This paper investigates the use of photon pressure and ablation from space-based lasers to directly affect the orbits of small debris fragments, both to lower their orbits and lifetimes, and to reduce collision risk with operational satellites. A mission concept is studied which enables the cataloguing of debris shells of small fragments produced after breakup events, while also allowing the encountered fragments to be illuminated by a laser on board the observation satellite(s). The concept takes advantage of a laser's ability to impart momentum at a distance by employing opportunistic interaction with passing fragments, assuming no prior knowledge of their orbits and no ability to rendezvous. The impact of the mission over a 10-year operational lifetime is simulated statistically by analysing the dynamics of typical encounters and the achievable impact on fragment orbits. The effects of off-beam-axis components of the applied ΔV and its implications for beam tracking are also investigated, along with the effects of extreme laser fluence on fragment attitude.

Keywords: Active debris removal; Laser ablation; Photon pressure

1. Introduction

With declining costs of space launches due to advances in launch vehicles reusability, the number of satellites in Earth orbit is likely to increase significantly over the coming years as space becomes more easily accessible and more widely exploited for commercial applications. As the density of satellites in orbit increases, the risk of collisions increases along with it. It is all but inevitable that more collisions will occur in the future, necessitating the development of effective, feasible and scalable debris remediation to ensure the long-term safety of the space environment in Earth orbit.

Satellite collisions (such as the Iridium-Kosmos collision of 2009), or the testing and eventual use of anti-satellite weapons - which have seen relatively frequent testing in recent years - result in the production of large numbers of debris fragments. Over moderate timescales, these spread into shells due to precession of the nodes (Pardini and Anselmo, 2011). Due to extremely low atmospheric density, debris orbits decay very slowly, with many fragments of the aforementioned Iridium-Kosmos collision still persisting in orbit some 13 years later. In the extreme, these debris shells have the potential to render their orbital altitude bands completely unusable for satellites, and also highly dangerous for launch vehicles to traverse until the

* Corresponding author.
E-mail address: massimiliano.vasile@strath.ac.uk (M. Vasile).

https://doi.org/10.1016/j.asr.2023.06.031
0273-1177/

shell naturally deorbits. For higher orbits, this is particularly concerning as the atmospheric drag is even weaker, and fragments take even longer to deorbit due to natural processes.

In the event of such a high-altitude collision, active removal would likely be necessary to clean up the orbital region due to the longer lifetime. However, the large number of fragments produced means that any proposed mitigation strategy which involves rendezvous, capture, and deorbiting would be impractical due to the huge propellant expenditure required for hundreds or thousands of orbit-matching maneuvers. Such strategies are better suited for the removal of larger, uncontrolled objects such as defunct satellites or spent upper stages. Very few strategies have been proposed which have the capability scale to large numbers of fragments, which is necessary to clean up the result of a collision if prevention is impossible.

Lasers enable the ability to transfer small amounts of momentum to an object at a distance, provided sufficiently powerful optics are available to track the fragment and allow accurate laser pointing, all without any need for orbit-matching maneuvers. Photon pressure has been proposed in multiple mission concepts as a means to apply a small perturbation to fragment orbits, potentially reducing the collision risk with another space object. One such example is LightForce (Yang et al., 2016), which employs multiple ground-based continuous-wave (CW) lasers which illuminate the target fragment over multiple overhead passes, compounding the along-track displacement. Mason et al. (2011) proposed another photon pressure-based concept for collision avoidance using a laser on the ground, and showed that collision risk could be substantially reduced using such an approach. Such ground-based strategies require that the fragments are large or bright enough to track optically from Earth's surface at distances above approximately 500 km. Additionally, these ground-based strategies have typically relied on multiple engagements with individual fragments to increase the displacement, which of course requires knowledge of the objects' orbits to re-engage at a later time.

Space-based platforms are able to circumvent some of the limitations of ground-based systems. Their advantages originate primarily from the lack of atmospheric attenuation, shorter distance to target (resulting in less beam divergence and higher fluence), particularly for those higher orbits in which the lifetime is long, and the possibility of for better alignment between the negative velocity vector and the applied $\Delta\mathbf{V}$ vector. Ground-based platforms suffer from a tradeoff between better beam alignment with the retrograde direction, and atmospheric depth traversed causing greater attenuation: when the fragment is near the horizon the beam is best-aligned, but also traverses the most atmosphere and longest distance, causing a far lower surface fluence. Additionally, ground-based platforms which require precise focussing must deal with complications due to atmospheric turbulence. However, since the size, weight and power restrictions are far more generous for ground-based systems, these disadvantages may be offset by simply constructing more powerful lasers. Vasile et al. (2010) proposed and modelled the use of both surface ablation and photon pressure from solar concentrators with a space-based platform which follows the targeted piece of debris. This work showed the capability of such a system to lower debris orbits from 800 km to 200 km in a few hundred days of operation, from where natural decay would fully remove the fragments.

Surface ablation is an alternative mechanism to photon pressure whereby an object's orbit may be influenced by a laser. Of the debris remediation strategies using ablation, L'ADROIT (Phipps, 2014) is one of the most well-developed space-based concepts, employing a single large satellite in an elliptical polar orbit between 560–960 km. L'ADROIT is in some respects similar to the concept proposed in this paper, utilising an opportunistic interaction strategy with passing fragments rather than targeting specific fragments whose orbits are known *a priori*. This paper builds on the L'ADROIT concept in several ways. Firstly, the altitude range targeted by L'ADROIT, as will be discussed in this paper, already has a relatively short natural lifetime for small fragments, making the potential return on investment limited - this paper instead targets higher orbits with a longer natural lifetime. Secondly, the analysis simplified the effects imparted $\Delta\mathbf{V}$ misalignment with the negative velocity vector, which this paper attempts to model in more detail.

This paper will present an analysis of the use of photon pressure and ablation from one or more space-based platforms, first for debris removal and then for collision avoidance. The key contributions of this paper which distinguish this work from previously mentioned space-based concepts like L'ADROIT (Phipps, 2014) and the work of Pieters and Noomen (2022) are the following. Firstly, a high-fidelity model of photon pressure and ablation was used to characterise the impulse transferred in a given interaction, rather than relying on simplifying assumptions. Secondly the proposed mission utilises a constellation of satellites rather than a single station. Thirdly, rather than following the debris and illuminating it continually as was proposed by Vasile et al. (2010), this concept uses short, opportunistic interactions with passing fragments. Finally, photon pressure was investigated as a means of debris remediation, from the aforementioned space-based platform.

This paper is an extension of previously published work by the authors (Walker and Vasile, 2021; Walker et al., 2021), in which this concept was initially introduced. This work builds on these papers in several ways - firstly by including analysis on the off-axis component of transferred momentum and its implications for beam tracking, secondly by extending the analysis of the collision avoidance scenario to include the expected encounter rate between a single object and satellites in a 10-satellite constellation. Finally, it adds new analyses on the effects of extreme laser fluence on the attitude motion of illuminated fragments to

determine if objects tend towards an orientation that reduces the net momentum transfer.

We first present an overview of the mission concept, and some initial analyses on orbital lifetime to justify a choice of altitude at which to focus the concept. Then, a process for generating orbital elements of a debris shell is described in Section 3, and the process of orbital propagation, encounter identification and downselection of candidate encounter events is described in Section 4. Section 5 describes the high-fidelity models of momentum transfer via photon pressure and ablation, and Section 6 presents the results of the full 10-year mission simulation for both cases. Following this, Section 7 discusses and simulates an adaptation of the concept to the goal of collision avoidance in the case of photon pressure, and finally Sections 8 and 9 analyze the effects of the laser interaction on debris attitude and lateral movement with respect to the beam axis.

2. Mission concept

The proposed concept is as follows. The targeted population of debris is those fragments in the sub 10 cm size range - those which are both numerous and often too small to be accurately tracked from Earth. A small constellation of satellites is inserted into a shell around the Earth such that the constellation has access to all longitudes. The target altitude would be chosen such that the satellites reside close to an altitude band which is particularly debris-dense. To mitigate the obvious collision risk of operating satellites in proximity to large numbers of debris, an orbit slightly higher than the peak of debris density may be chosen. Also, as will be discussed, this concept relies on optical tracking of fragments by on-board optics, and it is thus conceivable that an orbital catalogue of the debris shell may be built up over time, allowing for collisions to be anticipated and avoided.

Each satellite carries two primary instruments: a camera for acquisition and tracking of debris fragments, and a high-power laser, which is used to impart momentum to passing fragments. The scenarios of both CW and pulsed-mode lasers, using photon pressure and ablation respectively, is simulated.

Due to the high power consumption of the laser system combined with an expected low overall duty cycle, the laser is to be powered by a battery bank onboard the spacecraft, with sufficient capacity to power typical interaction events, and sufficiently-sized solar arrays to fully recharge in the typical duration between consecutive encounters. This battery bank and solar array could also serve to power low-thrust electric propulsion for orbit maintenance or adjustments, prolonging the lifespan of such satellites and enabling transfer to different orbits as needed.

The camera continually scans the sky in a cone behind the spacecraft, searching for fragments inside its field of view (FOV). When a fragment is identified, the laser is steered onto the target fragment to initiate an interaction, and tracks its movement across the sky. The aperture diameter of the lasers used in this concept is 20 centimetres to reduce the mass of the steering related components and overall optical system. No prior knowledge of the fragments' orbits is assumed as the premise of the concept is to be able to interact with small, untrackable fragments. Thus, fragments are acquired and interacted with opportunistically, as they pass through the camera's FOV.

An additional use of the camera which is not studied here is to reconstruct the orbits of the debris fragments that are encountered. Since this concept is aimed at smaller, untracked fragments, this data alone provides valuable information relating to collision risk and avoidance and could enable better cataloguing and collision prediction with small fragments.

Beyond the power system, no detailed attempt to estimate the size and mass of the individual spacecraft is made, however it is expected that these would be of the small-sat class, between 100 and 300 kilograms each. To launch a constellation of one hundred 300 kg satellites, two Falcon 9 launches would be required (SpaceX, 2021), costing $100 million with reused boosters. This assumes onboard electric thrusters are used to transfer from the delivery orbit to the operational orbit.

Since the net velocity change from photon pressure based interaction is expected to be small, an initial study was performed to assess the lifetime impact of small impulsive ΔV applications at varying altitudes to better target a given altitude band. Since lower fragments naturally deorbit more quickly, it is expected that more meaningful lifetime reductions could be achieved for higher orbits. However, as the orbit gets higher, the spatial density of debris and the subsequent interaction rate would lower for a roughly uniform shell. Thus this class of mitigation strategy should be targeted at orbits that are high enough to have relatively long lifetimes, while not being so high that the interaction rate becomes very low.

Orbits are propagated in this paper using a tool developed at the University of Strathclyde called CALYPSO (Di Carlo et al., 2021). CALYPSO propagates orbits semi-analytically, taking into account perturbations including atmospheric drag, third body and J2-J4 perturbations. However, for the sake of computational efficiency, orbit propagations in this paper are performed with drag as the only perturbation. This is a limitation of this study as the combined effect of zonal harmonics and light pressure would change the revisit time and also the eccentricity of the orbits of the fragments. For modelling atmospheric drag, the volume, size and area-to-mass ratio (AMR) from a 3D model of a 2 cm aluminium hex nut are used to represent debris fragments. The AMR of this 3D model is 0.3391. This coincides approximately with the peak of the distribution of the catalogued debris from the Iridium-Cosmos collision (Wang, 2010) and thus is a reasonable representation of a typical fragment produced in such a collision. The same 3D model is also used when simulating the laser momentum coupling.

Circular orbits of varying altitudes, inclined at 45 degrees were propagated until reentry. An initial impulsive $\Delta\mathbf{V}$ was applied in the negative velocity direction ranging from zero to 50 ms^{-1}.

The effects on the time-to-reentry can be seen in Fig. 1. It can be seen that, for higher orbits, a given $\Delta\mathbf{V}$ application results in a larger absolute lifetime reduction, as expected. For lower orbits, the reduction becomes less meaningful - for example for 700 km altitude, the expected lifetime is already under 10 years, so smaller $\Delta\mathbf{V}$ interventions may only reduce a fragment's life by a few months at best. For a 1200 km orbit, a smaller $\Delta\mathbf{V}$ has a more significant impact, with only 10 ms^{-1} reducing lifespan by over 10 years

Taking this into account, for the remainder of this paper we consider a case of 1200 km, 45 degree inclined orbits as the basis for this feasibility assessment.

3. Generation of the debris population

A debris population representative of that produced by a collision event must be generated to be used in this analysis. TLE data is available (CelesTrak, 2019) for the tracked fragments from the 2009 Iridium-Cosmos collision, which can be compared with the pre-collision orbits of the two satellites to assess how the cloud characteristics compare with the orbit of the satellites.

The TLE data showed that the altitude and inclination followed approximately normal distributions, close to the pre-collision values of the satellties. Inclination was very tightly clustered around the pre-collision value, with standard deviations of 0.051^o for the Iridium-33 cloud and 0.0326^o for the Kosmos-2251 cloud. Altitude was found to have dissipated more over time due to differential drag effects, with standard deviations of 76.4 km and 79.0 km.

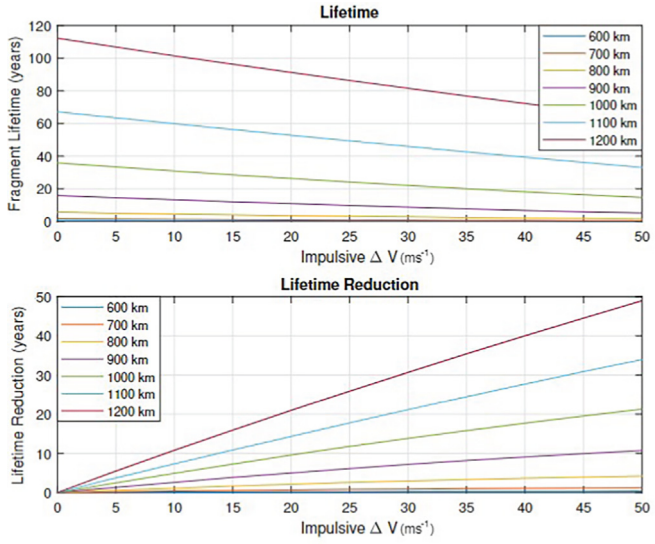

Fig. 1. Lifetime and lifetime reduction with an impulsive $\Delta\mathbf{V}$ for circular, 45 degree inclined orbits of varying altitude.

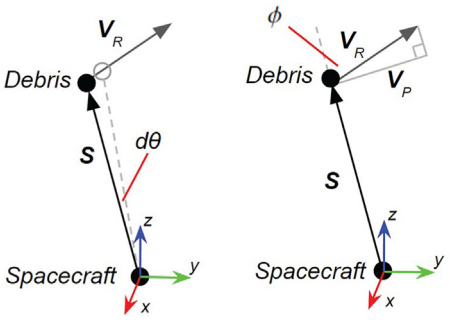

Fig. 2. Geometry of instantaneous relative angular velocity calculation. Over an infinitesimal time dt, the debris object traverses angular distance $d\theta$ from the point of view of the spacecraft.

The eccentricity distribution is observed empirically to follow a log-normal distribution, with no discernable relation between the satellite eccentricity and curve parameters. The right ascension of the ascending node and true anomaly had both dispersed to a quasi-uniform distribution (Pardini and Anselmo, 2011).

A set of debris orbits was generated based on these distributions to simulate the population which might be produced by the breakup of a satellite in a 1200 km circular orbit, inclined at 45 degrees. Altitude, inclination and eccentricity values were generated with the same distributions (normal and log-normal) found in those same values from the Iridium-Cosmos clouds, with distribution parameters equal to the average of the two clouds' distribution parameters. The other orbital elements were generated as uniform random numbers between 0 and 359.9 degrees, ie assuming that the cloud has already spread into a shell.

4. Encounter model and target acquisition

In order to determine the long-term impact of this mission concept, a quasi-statistical approach must be used due to the computational demand of propagating thousands of fragments and computing their interactions with the spacecraft. To achieve this, a small, representative population of 632 fragments is propagated over a 10-year mission span, as well as the orbit of a single satellite with semi-major axis 7571 km, zero eccentricity and 45 degrees inclination. Since the debris shell is uniform and the orbit is circular, the values of the other elements for the satellite have no effect and so are simply set to zero. Over the course of the 10-year duration, the satellite will have many close approaches with objects in the shell, whose dynamics will be extracted and passed to the laser coupling model to allow statistical generation of interaction events for a mission employing an arbitrary number of satellites.

Candidate encounters are identified by tracking the separation between the spacecraft and each fragment in the population over the 10 years. This separation oscillates, producing many local minima which are the initial candidates for interaction. These require more processing to remove non-encounters and infeasible encounters. These

candidate events are saved along with the states of the spacecraft and fragment at the instant of closest approach, in order to apply a series of conditions in a decision tree to determine if camera acquisition - and subsequently laser interaction - may be possible in each event.

Feasible candidates are selected from the initial set by applying two conditions at the instant of closest approach - firstly, the fragment must be visible to the camera, and secondly, the fragment must be within 30 degrees of the spacecraft's negative velocity direction, which is the centre of the FOV. Taken together, these ensure that the spacecraft and fragment are in similar orbits (large inclination differences would cause a high relative angular velocity and motion blur and thus these cases are removed in the visibility condition), and that the direction of the laser beam is reasonably well-aligned with the fragment's negative velocity direction (from the second condition). This also accounts for the limited field of view (FoV) of the camera.

The visibility condition is assessed by performing an SNR analysis using the camera system parameters and the dynamics of each individual candidate event. The limiting factor in the case of dim, moving objects is motion blur due to the image moving onto adjacent pixels before the required SNR can be reached. With no prior knowledge of the object's position, this effect is impossible to remove by camera panning. The condition for visibility then becomes that the minimum SNR must be achievable before the object image moves by one pixel width in the sensor plane.

The relative angular velocity profile of each candidate must now be calculated. In a reference frame centered on and co-moving with the spacecraft, with arbitrarily oriented axes, let $\mathbf{S}$ be the vector originating at the spacecraft and ending at the fragment. During imaging, $\mathbf{S}$ will also be aligned with the camera pointing direction. Let $\mathbf{V}_R$ be the velocity of the fragment relative to the satellite. $\mathbf{V}_R$ has a component perpendicular to $\mathbf{S}$, which we shall call $\mathbf{V}_P$ (the projection of the relative velocity onto the image plane), whose magnitude is $V_P = V_R \sin\phi$, where ϕ is the angle between $\mathbf{S}$ and $\mathbf{V}_R$. This is illustrated in Fig. 2. At any instant during the encounter, the instantaneous angular velocity can be found by considering the small change in angular position $d\theta$ which occurs over a small time dt:

$$\frac{d\theta}{dt} = \frac{V_R \sin\phi}{S} \tag{1}$$

where S is the magnitude of the vector $\mathbf{S}$.

4.1. Optical acquisition

Analysis on optical acquisition is performed by estimating the SNR of pixels containing the fragment compared with background pixels. SNR is here defined as the ratio of the mean signal photon count on a pixel containing the fragment μ_s, to the standard deviation of the noise counts in background pixels σ_n:

$$SNR = \frac{\mu_s}{\sigma_n} = \frac{\mu_s}{\sqrt{\mu_n}} \tag{2}$$

.

The expected, or mean, signal photon count per pixel per exposure, μ_s, can be derived from first principles, assuming isotropic hemispherical reflection from the fragment, and written as

$$\mu_s = \frac{\Phi_\odot \Delta\lambda A_F \alpha_F \lambda A_{col} \eta_c}{2\pi R^2 hc n_{px}} t_{exp} \tag{3}$$

where $\Phi_\odot$ is the solar irradiance, $\Delta\lambda$ is the bandwidth of the camera, A_F is the illuminated surface area of the fragment visible to the spacecraft, α_F is the albedo of the fragment in the chosen wavelength band, λ is the central wavelength of the CCD's sensitive band, R is the distance to the fragment, h is Planck's constant, A_{col} is the area of the light collecting optic, η_c is the overall photon-to-electron conversion efficiency of the entire camera-CCD system, t_{exp} is the exposure duration, and n_{px} a factor which approximates the effect of sub-pixel sized objects' convolution with the camera's point spread function (PSF).

Background, or noise, counts in a CCD typically consist of several sources - dark counts, non-image photons in the field of view, and readout noise. In this case, we assume negligible non-image photons, as observations will not be made while the Sun is in the field of view, the aperture would have a sun-blocking baffle, and the camera will be kept pointed above the horizon, with the Earth also outside of the field of view. Thus the noise is dominated by dark noise and readout noise. The mean noise photon count *per pixel* can be written as

$$\mu_n = Dt_{exp} + R \tag{4}$$

where D is the mean dark count rate per pixel, and R is the mean readout noise per pixel per exposure. In space-based CCD imagers, sub-100 Hz/px dark count rates have been demonstrated with active cooling, with around 10 Hz/px being achievable at temperatures of −30 Celsius (Gilard et al., 2010). Given the large capacity power delivery and storage systems that will be required for the laser system on board each satellite for this mission, it is reasonable to assume CCD active cooling will be available to reduce dark count rate to the 10 Hz/px level, so this is the level used in the base case calculations.

The condition for the object to remain on the same pixel for the duration of a single exposure is

$$\frac{d\theta}{dt} t_{exp} \leqslant \theta_{px} \tag{5}$$

where θ_{px} is the angular size of a camera pixel. To combine this with the SNR requirement and determine if visibility is physically possible, t_{exp} must also be greater than the minimum required exposure t_{min} for the chosen SNR threshold at that instant, calculated from Eqs. 2,3. In other words, for visibility to be possible, there must be some t_{exp} which is both short enough to satisfy Eq. 5, and long enough to

accrue the desired SNR. The exposure duration is considered to be variable, by use of frame stacking, and no set value of t_{exp} is chosen here. These conditions are checked at each time point near an encounter to determine at which points, and for how long, the fragment can be tracked by the camera and laser. An example of this can be seen in Fig. 3, with the orange line indicating the time section of the encounter when both conditions are fulfilled - ie the window during which the laser can affect the target.

Fig. 4 shows the minimum required exposure for various SNR thresholds as a function of distance from the fragment, using the parameters in Table 1.

The illuminated area chosen in these calculations was that of the 3D model of the hex nut (Fig. 5), along the direction of the axis passing through the central hole.

From the analyses in this section it is possible to extract information on all simulated encounters and construct distributions of key parameters such as interaction duration, time between successive encounters, and net impulse transfer vectors. This will be used in Section 6 to statistically generate encounters and their net impulse vectors in a local reference frame, so that the full 10-year mission may be simulated more quickly. Doing this on a per-satellite basis also allows different numbers of satellites to be simulated with the same distributions, all without using the computationally expensive LDI simulation. The mean time between events is 41802 s, or on average 0.483 encounters per day. When scaling up from the smaller population of 632 fragments to a more realistic population of 5000, the expected event rate is approximately 4 encounters per day, per satellite. This high encounter rate suggests that the rate of interaction is likely to be limited by the power system and not the encounter dynamics.

5. High-fidelity momentum transfer models

In order to quantify the force being applied to the fragment, a high fidelity model of photon pressure over 3D shapes was developed. The model takes a user-defined 3D model of a debris fragment, triangulates the surface and determines which portions of the surface are illuminated at each instant. It then calculates the net force and torque vectors (due to either photon pressure or ablation) at each timestep. This is used to update the velocity and rotation state and incrementally integrate the impulse over the course of the interaction to obtain the net momentum transfer vector.

After the 3D model has been triangulated, the illumination state I of each element must be determined to allow force calculation. This effectively modifies the area of the element to account for full, zero, or partial illumination. This is done by using the hidden point removal algorithm (Katz et al., 2007) to determine the visibility of each point in the 3D model point cloud, from the point of view of the laser. Then, for each element, an illumination state I is assigned depending how many of the three vertices are illuminated. For example, if no vertices are illuminated, $I = 0$, and if two are illuminated then $I = \frac{2}{3}$.

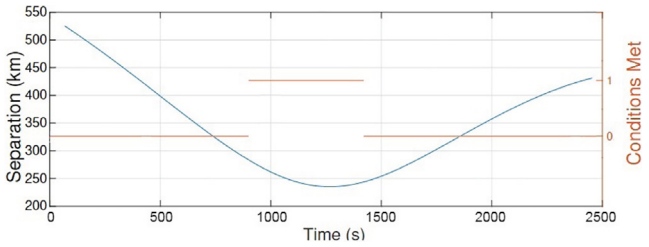

Fig. 3. Example of information extracted on the dynamics of a single encounter. The orange curve (right axis) is the binary condition where 1 denotes the fragment is observable at that instant. The full states of both the satellite and fragment are extracted from each encounter.

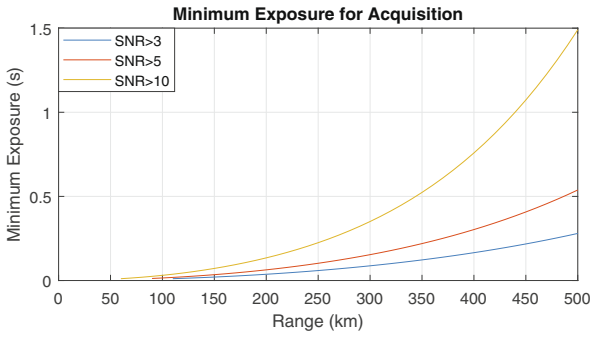

Fig. 4. Minimum required exposure at a given range to achieve the specified SNR.

Table 1
Parameters used for SNR analysis.

Parameter	Value
Camera Aperture Diameter	20 cm
Fragment Albedo	0.5
Camera Efficiency	40%
Central Wavelength	550 nm
Bandwidth	350 nm
Solar Irradiance	1.5 $Wm^{-2}nm^{-1}$
Debris Illuminated Area	2.034e-4 m^2
PSF size	4 pixels
Dark Count Rate	10 Hz px^{-1}
Mean Read Noise	5 counts $exposure^{-1}$ px^{-1}

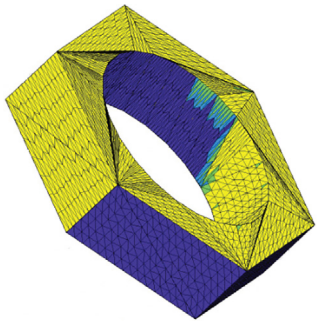

Fig. 5. Hexnut model used to represent typical debris fragments. Colour represents illumination state of surface elements.

The algorithm finds the net force and torque by integrating contributions over each surface element at each timestep:

$$\mathbf{F}_{net}(t_i) = \sum_{e=1}^{N} \mathbf{F}_e(t_i) \tag{6}$$

where t_i denotes timestep i, N is the total number of elements in the 3D model and $\mathbf{F}_e$ if the net force on element e calculated using the below equations for either photon pressure or ablation. Torque is calculated by taking the cross product $\mathbf{F}_e \times \mathbf{R}_e$, where $\mathbf{R}_e$ is the vector connecting each element's center (mean of the vertices) to the object's center of mass, and then taking the sum across all elements. From here, the rotation state of the object is propagated to the next time step by integrating Euler's rigid body equations using the inertia tensor of the 3D model. Short time steps of 0.1 s are used for each integration, during which the torque is held constant.

5.1. Photon pressure force model

When light is incident on a surface, some fraction is absorbed and the remainder is reflected. The reflected component can be further divided into diffuse and specular components - in diffuse reflection, photons are scattered according to Lambert's cosine law. In specular reflection, distinct rays of light reflect from the surface like a mirror, obeying Snell's law. For metallic space debris, the specular component is likely to be non-negligible, and so in order to accurately calculate the net momentum transfer, all three components must be included:

$$\mathbf{F}_e = \mathbf{F}_{specular} + \mathbf{F}_{diffuse} + \mathbf{F}_{absorption} \tag{7}$$

.

For the diffuse component, the reflection is axisymmetric about the local normal, so all transverse components cancel. Thus the net force will be in the direction of the local anti-normal, and its magnitude can be calculated by integrating the normal component of reflected light power across a hemisphere. Upon completing this integration, one obtains:

$$\mathbf{F}_{diffuse} = -\frac{2\alpha(1-S)P_{inc}}{3c}\hat{\mathbf{n}} \tag{8}$$

Here $\hat{\mathbf{n}}$ is the local normal unit vector, S is a factor between 0 and 1 which determines the fraction of light that is reflected specularly, α is the total reflectivity of the material. $\hat{\mathbf{n}}$ is the unit normal vector of the surface element, and c is the speed of light. P_{inc} is the total power incident on the element of area A_e accounting for the local incidence angle θ:

$$P_{inc} = \Phi(z)\cos\theta \tag{9}$$

Here $\Phi(z)$ is the laser power density at distance z from the emitter. For the specular component, the net force is simply equal to

$$\mathbf{F}_{spec} = -\alpha S\frac{P_{inc}}{c}\hat{\mathbf{r}} \tag{10}$$

where $\hat{\mathbf{r}}$ is the unit vector of the direction of the reflected light. Finally, the force on the surface element due to absorption is

$$\mathbf{F}_{absorption} = \frac{P_{inc}}{c}\hat{\mathbf{i}} \tag{11}$$

where $\hat{\mathbf{i}}$ is the direction of the incident light. Eqs. 8, 10 and 11 were obtained by the author's derivation from first principles consistent with similar approaches found in literature Bhattarai et al. (2022), Ziebart and Dare (2001). Full derivations of these 3 components may be found in the Appendix

5.2. Ablation force model

In ablative coupling, momentum is transferred to the target object by vapourising a small amount of surface material by use of high-energy laser pulses. The expanding plume of gas and plasma then produces a force on the fragment. The strength of this coupling in Newtons per joule has the potential to be several orders of magnitude stronger than that of photon pressure with sufficient energy and power density on the target surface.

The impulse transferred per surface element $\Delta\mathbf{p}_e$ is integrated element-wise similarly to the photon pressure model, with:

$$\Delta\mathbf{p}_e = -A_e\Phi_e C_m(\Phi_e)\hat{\mathbf{n}}_\mathbf{e} \tag{12}$$

where each element is denoted by e. Here Φ_e is the energy density on element e, dependent on the distance from the emitter and angle of the surface, and $C_m(\Phi_e)$ is the momentum coupling coefficient. It is unlikely that sufficiently high-powered lasers will be able to be launched into space to achieve the required fluence for ablation to occur without the use of focussing optics, so in the case of ablation it is assumed that variable-focus optics are able to track fragments longitudinally with the focal plane of the beam. This would in turn affect the requirement on emitter size, however, as achieving a 10 cm spot at 200 km range would require an aperture radius of 1.32 m. Assuming beam tracking, a constant value of C_m close to the optimal value is assumed to be achieved. The value used is $C_m = 20$ NsJ^{-1}, which represents the average for all available data in the literature for aluminium in vacuum at the relevant pulse duration (Phipps et al., 2004; Phipps et al., 2017; Wang, 2017; Tran et al., 2017). It should be noted that C_m varies significantly between materials - aluminium was chosen as a representative material here due to the relative abundance of experimental data in the literature while also being a common material in spacecraft construction. This model is flexible and could be adapted to simulate any desired geometry and material, so long as material parameters are changed accordingly. A more complete analysis would include a wide variety of object of different sizes,

shapes and materials, distributed according to the results of a satellite breakup model.

5.3. Longitudinal laser profile

As previously mentioned, for the photon pressure case this concept does not assume the availability of ranging measurements and variable-focus beams. This section will discuss optimisations of the focal plane location and waist radius to maximise the irradiance delivered to fragments during interactions.

For a Gaussian, near-single-mode beam, the minimum possible beam divergence is $\theta_d = M^2 \frac{\lambda}{2\pi w_0}$, where λ is the laser wavelength and w_0 is the beam waist radius - the radius of the most tightly focussed point along the beam axis. The factor M^2 (greater than or equal to 1), known as the beam quality factor, captures any deviation from a perfectly Gaussian beam profile. A moderately divergent beam with $M^2 = 1.8$ was assumed in this paper, as such a high-powered laser is likely to be a multi-mode beam (due to for example thermal effects limiting the maximum optical power density (Jauregui et al., 2013)) which cannot have divergence very near to the theoretical minimum. Higher beam quality would allow greater fluence to be delivered to the target. $\lambda = 1064$ nm is used in this paper, corresponding to common Nd:YAG laser technology.

From this, simple geometry allows the beam radius $w(R)$ at any given longitudinal distance from the focal plane (or beam waist) to be calculated:

$$w(R) = w_0 + \sqrt{(R - z_0)^2}\tan(\theta_d) \tag{13}$$

Here R is the distance from the emitter, w_0 is the waist radius, and z_0 is the focal plane's distance from the emitter - thus the term $\sqrt{(R - z_0)^2}$ is the distance of the point of interest from the focal plane.

The simplest approach would be to simply have the waist radius at the emitter, or $z_0 = 0$. However, since this concept deals with long ranges and the effect of the interaction depends strongly on the irradiance incident on a fragment's surface, alternatives should be explored that allow for higher irradiance to increase effectiveness and/or reduce laser requirements.

It is important to note that z_0 cannot be arbitrarily chosen, but is constrained by the maximum size of the emitter on board the spacecraft. The required emitter radius can be obtained from Eq. 13 by setting $R = -z_0$. Fig. 6 shows the relationship between desired waist radius and required emitter size, with z_0 fixed at several values.

It can be seen that larger emitters allow the waist to be placed further away from the craft, and thus a higher fluence to be delivered to the target. A constraint on the size of the emitter must exist since it must fit on board the spacecraft, but precisely defining this is outwith the scope of this paper. An approximate upper limit of $w_e = 0.2$ m was chosen to constrain the parameters z_0 and w_0. Since

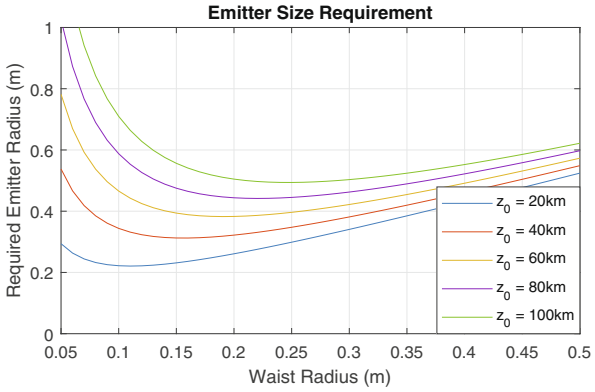

Fig. 6. Emitter size requirement for various z_0 and w_0.

long distance interactions are required, it is desirable to have the focal plane as far from the spacecraft as possible for a given emitter size to maximise the fluence at the target. To find this maximum possible z_0 and corresponding waist radius, z_0 is reduced until the turning point of the curve (similarly to Fig. 6) occurs at an emitter radius of 0.2 m. The optimal focal plane distance was found to be $z_0 = 15.59$ km with a waist radius $w_0 = 0.1$ m. These optimal parameters are used in the laser-debris interaction modelling in later sections.

5.4. Momentum transfer calculation

The database of encounters and their dynamics obtained in Section 4 is now used to model the interaction of the laser beam with the fragment and obtain a net impulse transfer for each encounter. This allows a database of several thousand interaction results to be calculated, to be drawn from when simulating the mission impact. A total of 7549 viable encounters were extracted from the orbital propagation and used to build this database.

An example of the dynamics extracted from a single encounter can be seen in Fig. 3, where the orange line is a binary state of observability (all criteria being met) for that instant in time. Thus, only the dynamics during periods where this condition equals 1 are fed into the photon pressure model. The distribution of visibility window duration can be seen in Fig. 7.

The separation vectors $\mathbf{S}(t)$ during the observable window for each encounter are passed into the laser-debris

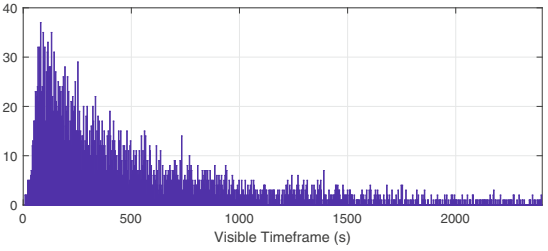

Fig. 7. Distribution of visibility window duration.

interaction (LDI) model described previously for photon pressure. This integrates the laser pressure force over the course of the interaction, accounting for variability in the direction of incidence and magnitude of irradiance over time due to changes in the distance to the laser source. The laser power was modelled as 10 kW optical (33.3 kW total power draw if 30% efficiency can be attained).

The LDI model outputs a single vector which represents the net $\Delta\mathbf{V}$ accrued over the entire interaction. The direction of the impulse is expressed in a local reference frame for each encounter so that the net $\Delta\mathbf{V}$ vectors may be applied to other encounters. The local reference frame used has its origin at the location of the at the distance-weighted mean time of the observability window. The direction of the net $\Delta\mathbf{V}$ vector is expressed in terms of its magnitude, declination and right ascension relative to the negative velocity direction of the fragment.

Building this database allows encounters to be 'generated' by selecting a random scenario from the database, and applying that scenario's $\Delta\mathbf{V}$ impulsively to the state of the fragment in question, without having to run the computationally expensive LDI model. Selecting individual encounters from a large enough database to be reused ensures that any statistical correlations between the dynamics of the encounter and the resultant net impulse are preserved.

6. Debris deorbiting

Using the results of all previous sections, we are now able to assess the effectiveness of a constellation of satellites deployed into a debris shell as a response to a breakup event.

To achieve this, a new set of 5000 fragments is generated in the same way as before, centered around the same 1200 km altitude.

Satellite orbits are not propagated explicitly in the mission simulation. Instead, interaction times are generated from the previously found distribution of consecutive event separations, scaled up to the larger population, until a full 10-year mission duration's worth of encounters has been generated for a single satellite. For each interaction, a random fragment identifier number is assigned, which is the fragment that is encountered in that instance.

This is repeated for each satellite in the constellation - 100 in the base case - and all events together with their timestamps, fragment identifiers and satellite identifiers are collated into a single database. Exactly half of these events are then randomly selected and removed, to account for eclipse conditions where the Sun does not illuminate the fragment, rendering it invisible to the camera. Finally, for consecutive events involving the same spacecraft where the time separation is insufficient to recharge the batteries using solar power, only the first encounter is kept.

Fragments' orbits are then individually propagated from $t = 0$ to each subsequent interaction time. Here, an impulsive $\Delta\mathbf{V}$ - whose magnitude and relative direction are taken from a randomly selected encounter from the database built in Section 5.4 - is applied to its state vector before it is propagated to the next encounter. We account for uncertainty in the size and material composition of different fragments by multiplication of the $\Delta\mathbf{V}$ by a pair of fragment-specific scaling factors - one for physical size d and one for deviations from the C_m of aluminium caused by impure or differing surface materials. This is possible because the previously derived equations in both cases are proportional to powers of d, or directly proportional to C_m. The distributions of d and the C_m scaling factor can be found in Fig. 8. After the final encounter has been reached, the fragment's orbit is then propagated to the end of the 10 year mission span with no further interaction perturbations. The original orbit is also propagated unperturbed for the full 10 year duration to identify changes due to the applied interactions.

Fig. 9 shows the distribution of periapsis change for each fully propagated fragment in the population, in the case of photon pressure. In these results, only 1000 fragments have been propagated to the end of the 10 year mission duration to gain an insight into the expected effect on any given fragment in the population. As can be seen, the expected change in periapsis is small, with a mean reduction of only 38.7 metres. Lifetime reduction was assessed and found to be negligible. This result indicates that the effect of photon pressure from space-based platforms is not strong enough to have any meaningful impact on fragment lifetimes.

The same mission simulation was preformed for the ablative interaction mode. To build the equivalent database of interaction effects as for photon pressure, 300 pulses of 3 kJ (total optical energy 0.25 kWh) were simulated at a random time point within the each visibility window. This is because no assumption is made of range knowledge which could be used to maximise the fluence. A limited number of pulses was simulated since the laser will be powered by batteries with limited capacity and

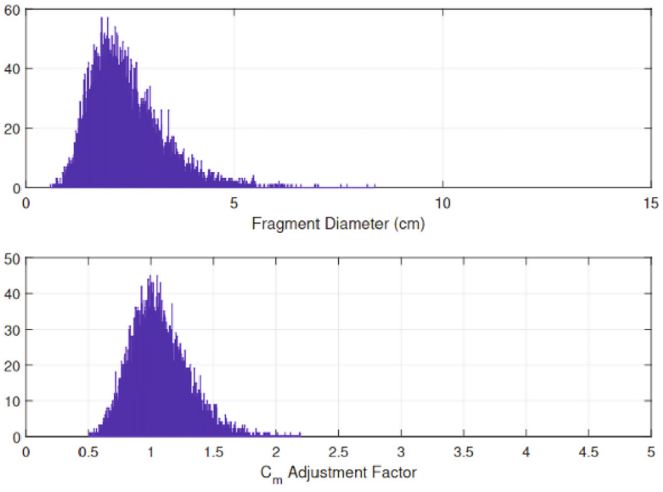

Fig. 8. Distribution in fragments' diameter d and C_m scaling factor.

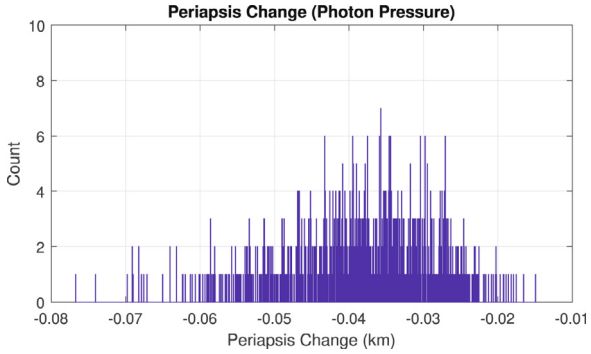

Fig. 9. Net change in periapsis for 10 year mission duration using photon pressure for 1000 fragments. Mean periapsis reduction was 38.7 metres.

could likely not operate continuously for several minutes, both due to power draw and heat buildup, which will both be more significant than the CW case. A waist radius of 0.1 m, as in the photon pressure case, was used for ablation simulations.

Total power draw and instrument mass are difficult to estimate in the case of the pulsed system, since few kilojoule-level pulsed systems have been constructed, with none intended for space application. The mass, power draw and efficiency of pulsed systems depends heavily on many design factors including gain medium, number of amplification stages and architecture used to create pulses such a Q-switching, modulated diode amplification etc. The L'ADROIT concept (Phipps, 2014) estimated an overall electrical-optical efficiency of 32% based on the performance of the 7 kJ, 18 Hz LIFE laser combined with knowledge of technology improvements in the years since, which we take as an estimate of the efficiency in this case. Assuming the same repetition rate of 18 Hz, the system would draw 54 kW average over 16.7 s to transmit the train of 300 pulses. The total energy drawn from the storage system would be 0.781 kWh. For a 50% beginning-of-life depth of discharge and an energy density of 338 Whkg^{-1} (corresponding to that of modern 4680 cells designed for electric vehicles), this would require a battery mass of 4.62 kg. A m^2 solar array operating at 30% efficiency would be sufficient to fully replenish this energy draw in 22.8 min. This is achievable in a single orbit, allowing as well for panel performance degradation over the mission duration.

Due to the stronger momentum coupling, as expected this mode of interaction induced a much stronger effect on fragments' orbits and lifetimes than the photon pressure case. Results for the change in periapsis and lifetime can be found in Figs. 10 and 11 respectively. It can be seen that in the ablation case, the lifetime reduction is measured in decades and periapsis reduction of over 100 km is achieved in all cases.

7. Photon pressure for collision avoidance

Despite the poor potential to lower a fragment's orbit via photon pressure, this interaction mode may still have

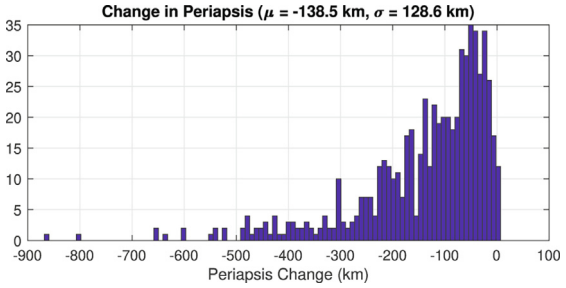

Fig. 10. Periapsis change for propagated fragments in the ablation case.

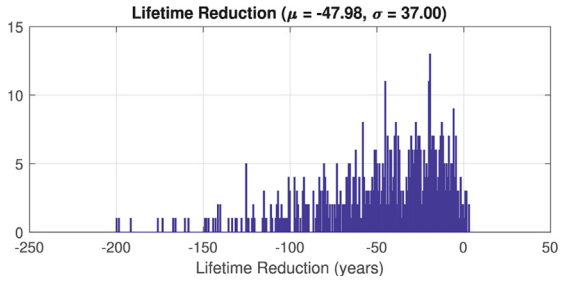

Fig. 11. Lifetime change for propagated fragments in the ablation case. Some fragments have already re-entered in the 10-year mission span.

some application for collision avoidance, which allows a very small perturbation to a fragment's velocity to compound over time, resulting in a large position change.

To investigate this possibility, random fragments were selected from the population used previously and propagated for some shorter time t, both with and without a single impulsive interaction applied at $t = 0$ in order to assess the magnitude of the effect by comparing the position of the fragment at the end of the propagation period. The results of this for 500 different fragments and impulsive interactions after a 1 day collision notice period can be found in Fig. 12. With only a single interaction, for the chosen laser parameters and this fragment's area-to-mass ratio, it is possible to achieve an along-track displacement of several hundred metres with one day of advance notice of a collision.

This analysis was repeated for several different notice periods. The results of this can be found in Fig. 13, showing that with sufficient notice period, a displacement of sev-

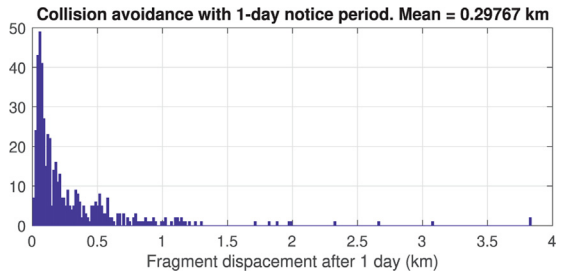

Fig. 12. Fragment displacement w.r.t unperturbed position after 1 day (500 encounters).

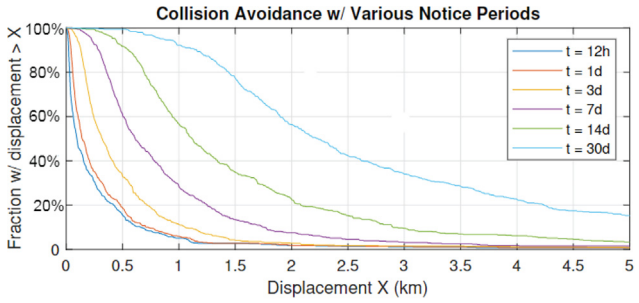

Fig. 13. Fraction of fragments where a minimum displacement is achieved after various notice periods up to 30 days.

eral kilometres with respect to the unperturbed position could be achieved.

Fig. 14 shows the distribution of the angle of the deviation with respect to the fragment's negative velocity vector after one day, showing tight clustering around zero, indicating that the fragments are being temporally displaced to avoid a potential collision, even with sub-optimal beam alignment with the negative velocity vector of the fragments.

To investigate the feasibility of this adaptation of the concept, the orbits of a 10-satellite constellation were simulated along with that of a randomly generated, single fragment with the same statistics as previously, to investigate the encounter rate between the fragment and any satellite in the constellation. The satellites were initialised in an evenly spaced orbital shell, with identical a, e, i and ω, and with Ω and ν spanning 360 degrees in increments of 36 degrees. Orbits of all bodies were propagated for one day, and the separation between the fragment and each satellite was tracked. An example of this can be seen in Fig. 15, where each curve represents the distance to one of the satellites in the constellation.

With this constellation of only 10 satellites, it was typical to observe a closest approach of < 200 km within a one day timeframe, which is a typical range for the fragment during an interaction window. Results for the closest encounter with any satellite in the constellation in one day across 500 randomly generated fragments are shown in Fig. 16.

The time until the first approach closer than 200 km with any satellite is also shown in Fig. 17. 90% of the sub-200 km encounters occur in less than 27.3 h, and 95% occur in less than 36.8 h.

This indicates that with a very reasonably-sized constellation of 10 satellites, fragments in the vicinity of the constellation's orbit can be expected to approach close enough to one of the satellites to be nudged by the illumination laser within two days of identification of a threat. Unless the notice period is very short, it is likely that a fragment will in fact have multiple encounters with satellites before the moment of the potential collision. This indicates that this concept may indeed have potential to be adapted for the purposes of cataloguing debris fragments in the vicinity of high-value stations and intervening should a collision risk be detected.

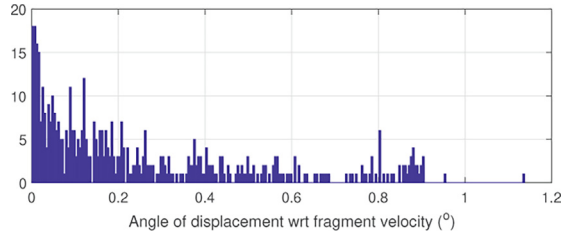

Fig. 14. Relative angle of displacement showing clustering in the along-track direction. 1 day notice period, 500 encounters.

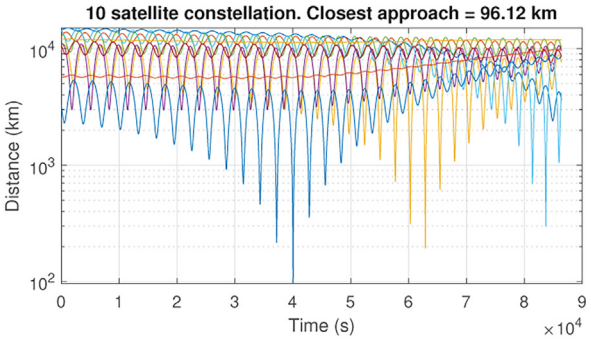

Fig. 15. Magnitude of separation between a fragment and each satellite in a 10-satellite constellation over one day. Each curve represents the distance to one of the satellites in the constellation.

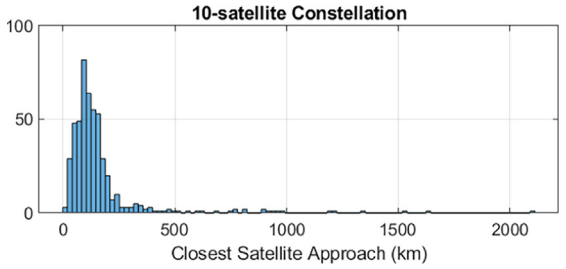

Fig. 16. Closest approach with any satellite in the constellation for 500 randomly generated fragment orbits after one day.

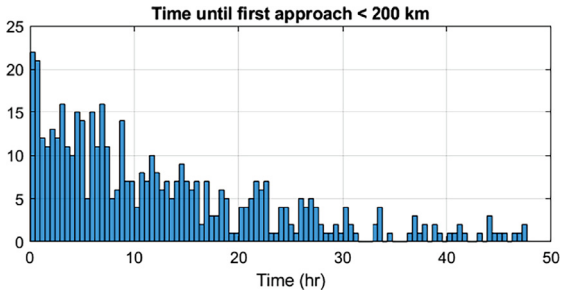

Fig. 17. Time until the first encounter with any satellite closer than 200 km.

8. Effect of laser illumination on debris attitude

One concern when considering high-power photon pressure or ablation-based interactions relates to the evolution of the attitude of the fragment over the course of an interaction period. A reasonable hypothesis is that fragments may, depending on their geometry, tend towards an orientation state that minimises torque, much like an aerodynamic situation. This was investigated using the high-fidelity model for photon pressure, with the laser power raised to an extreme level to accelerate the effect. This is also a good approximation for the ablation case, in scenarios where pulses are rapid.

When considering a thin, square aluminium plate with light incident at an angle $\frac{\pi}{4}$ radians to the local normal on one face, naively one would expect a net torque of zero, since the surface fluence is simply $\Phi_0 \cos\frac{\pi}{4}$ at all locations. However, in the high-fidelity model there are small tangential components to the reaction force on a surface element, which should result in a net torque for those combinations of α and S that do not cause the tangential components to cancel.

8.1. Attitude dynamic model

Attitude motion is propagated according to a standard model of rigid body motion which will be summarised here. The net external torque $\boldsymbol{\tau}$ due to the laser illumination is simply the sum over all elements e of the contribution due to each element:

$$\boldsymbol{\tau} = \sum_e \mathbf{F}_e \times \mathbf{r}_e \tag{14}$$

where the vector $\mathbf{r}_e$ connects the object's centre of mass to the geometric centre of element e, expressed in the body frame. In the same body frame, the rate of change of angular velocity can be calculated according to Euler's equations of rigid body dynamics (Chobotov, 2008):

$$I_x\dot{\omega}_x + (I_z - I_y)\omega_y\omega_z = \tau_x \tag{15}$$

$$I_y\dot{\omega}_y + (I_x - I_z)\omega_z\omega_x = \tau_y \tag{16}$$

$$I_z\dot{\omega}_z + (I_y - I_x)\omega_x\omega_y = \tau_z \tag{17}$$

where $I_{x,y,z}$ are the principal components of inertia (in the body frame), $\tau_{x,y,z}$ are the three components of the vector τ, and $\omega_{x,y,z}$ is the angular velocity about the three principal axes, again in the body frame. The full angular velocity vector in the body frame is defined as ω_b.

The orientation of the body frame (and hence the object) with respect to the inertial frame is expressed by a quaternion $q(t)$, whose rate of change can be calculated according to:

$$\dot{\mathbf{q}}(t) = \begin{bmatrix} \dot{q}_1 \\ \dot{q}_2 \\ \dot{q}_3 \\ \dot{q}_4 \end{bmatrix} = \frac{1}{2}\begin{bmatrix} 0 & -\omega_x & -\omega_y & -\omega_z \\ \omega_x & 0 & \omega_z & -\omega_y \\ \omega_y & -\omega_z & 0 & \omega_x \\ \omega_z & \omega_y & -\omega_x & 0 \end{bmatrix}\begin{bmatrix} q_1 \\ q_2 \\ q_3 \\ q_4 \end{bmatrix} \tag{18}$$

(Chobotov, 2008).

8.2. Laser-induced torque

The size of this effect was investigated in the case of the aforementioned square plate, with dimensions 10 cm side and 5 mm thickness, a mass of 135.5 grams and constant density of 2710 kgm^{-3}. Its principal components of inertia are $I_x = 2.258 \times 10^{-2}$ $\text{kgm}^2, I_y = 1.132 \times 10^{-2}$ kgm^2, $I_z = 1.132 \times 10^{-2}$ kgm^2. With an extreme surface fluence of 1 TWm^{-2}, the angular acceleration about the torque axis was only 8.83×10^{-13} rads^{-2}. This indicates that for the flat plate, there is no strong restoring force which tends to bring the object into any preferred orientation. Note that we intentionally use extreme fluence values in order to induce large effects on the object attitude on the timescale of several minutes of simulation time. Given a longer simulation period the authors would expect to see similar effects emerge over time.

More complex geometries were simulated as well - firstly, an L-shaped block. For this object it was found that there exist certain 'metastable' orientations (such as the one illustrated in Fig. 18), where upon initialisation with zero angular velocity, under extreme fluence the object initially remains almost motionless. However, with very small deviations from this state, the orientation begins to oscillate with increasing amplitude before being thrown into a tumbling motion. An example of the time evolution of the angular velocity magnitude can be seen in Fig. 19. For cases with a random slow initial tumble, over many simulations no attractor states of orientation were identified. For these finite-time simulations, the direction of the incident light with respect to the inertial frame was held constant. Finally, the same hexnut model as previously was also simulated, resulting in similar findings to the L-shape, although a preference for spin-up about the short axis was observed, with the short axis angled with respect to the beam axis. This could be considered as an attractor

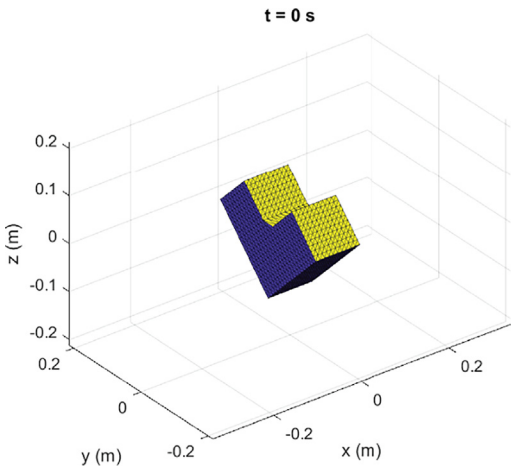

Fig. 18. L-shaped block in a metastable orientation under ultra-high fluence (10 GW m^{-2}) photon pressure.

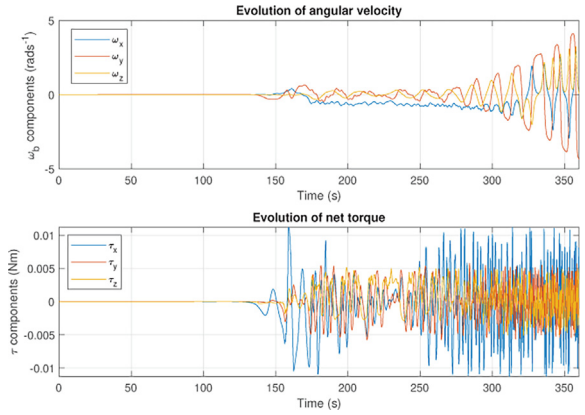

Fig. 19. Time evolution of angular velocity and net torque components for the L-shaped block under extreme laser fluence (10 GW m^{-2}), starting from the metastable state in Fig. 18.

state in the case of the hexnut, with respect only to the direction of the short axis. Time evolution of angular velocity and torque magnitudes for the hexnut can be found in Fig. 20.

These results indicate that under extreme CW illumination, or high repetition rate pulsed interactions, there will be no tendency towards a preferred orientation which minimises the force applied - rather there is a tendency for the spin-up of more complex objects. However, the effect is small, and only manifested when using unreasonably extreme fluence, and thus is unlikely to be a concern in the case of realistic fluences with photon pressure.

9. Lateral movement of fragments during ablative interaction

For complex geometries, the net force from ablation will not always be parallel with the beam axis. Since the impulse from a single pulse can result in a meaningful change in velocity for a small, light object, if this effect causes large sideways movement of the fragment relative to the beam direction, beam steering to ensure the target remains illuminated may become an issue.

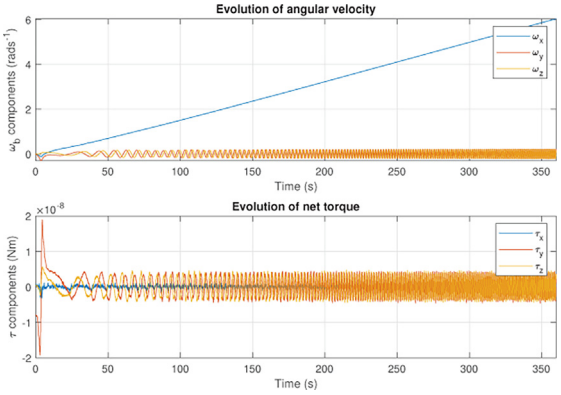

Fig. 20. Similar spin-up behaviour observed with the hexnut 3D model under a lesser fluence of 0.1 GW m^{-2}. Continual spin-up about the short axis was observed for the hexnut.

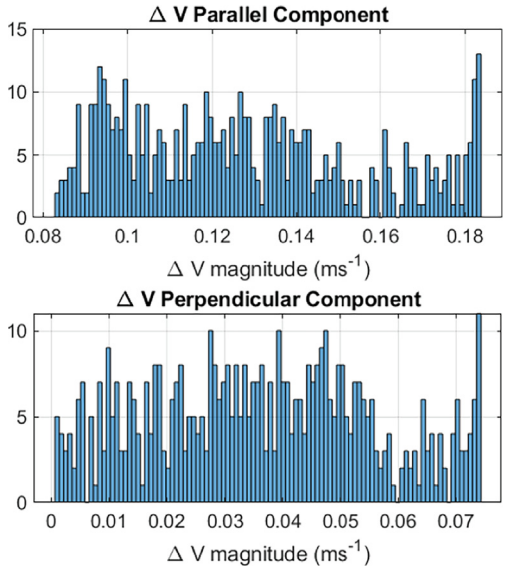

Fig. 21. Components of the resultant impulsive $\Delta\mathbf{V}$ from ablation with respect to the beam axis direction for the hex nut.

This effect was investigated by performing a Monte-Carlo simulation of 500 single-pulse interactions (4.4 kJ pulses focussed to a spot of radius 10 cm to achieve the optimum 14 Jcm^{-2}) on the hexnut model, where each simulation initialised the hexnut in a random orientation. The resultant $\Delta\mathbf{V}$ vector is computed according to

$$\Delta\mathbf{V} = \frac{1}{m_{frag}} \sum_{e} \Delta\mathbf{p}_e \tag{19}$$

where m_{frag} is the mass of the fragment and $\Delta\mathbf{p}_e$ is the element-wise impulse from Eq. 12. The interior volume of the hexnut 3D model was 9.432 $\times 10^{-7}$ m^3, and assuming the density of aluminium (2710 kgm^{-3}), $m_{frag} = 2.6 \times 10^{-3}$ kg. This was decomposed into its components parallel with, and perpendicular to, the beam axis. The results of these simulations can be seen in Fig. 21, which shows a significant component of the $\Delta\mathbf{V}$ indeed acts perpendicular to the beam axis for all cases.

This indicates that upon initiation of ablative interaction, a fragment will deviate significantly from its unperturbed path across the sky relative to the spacecraft. Thus a concern for the actual implementation of laser ablation of space debris is the ability to track the fragment as it takes a seemingly random path across the field of view, being kicked in a new direction by each consecutive pulse.

10. Discussion and conclusions

In this paper, a new mission concept was proposed and simulated to determine the feasibility of reducing the lifetime of a large population of small debris fragments using both photon pressure and laser ablation from space-based platforms. A high-fidelity model of both photon pressure and laser ablation was developed, and the mission was simulated using a debris population with similar orbital ele-

ment distributions as found in the Iridium-Cosmos shells. The results indicate that photon pressure fails to lower orbits significantly even when using a space-based platform. The mean change in periapsis achieved in the simulations was effectively zero, even for a 100-satellite constellation each carrying a 10 kW CW laser. Results for the ablation case showed more promise, however, indicating that it may be possible to achieve lifetime reduction of several decades for fragments orbiting at 1200 km altitude. This indicates that laser ablation from a space-based platform pay present a viable solution for removal of debris from satellite breakup events in the high-LEO altitude range.

As part of this analysis, we have shown that it is possible to optically acquire small (2 cm) fragments of debris in orbit using a small camera with no *a priori* knowledge of individual orbits. While visibility is dependent on the exact dynamics and illumination conditions of each individual encounter, a sufficiently large number of the simulated encounters had conditions favourable enough to facilitate optical tracking. This presents the possibility of a secondary mission objective or standalone concept in which the goal is to catalog the fragments in such a cloud for the purposes of collision avoidance.

While photon pressure was shown to be ineffective for orbit lowering, we have shown that it still has potential for collision avoidance, with an along-track displacement of several kilometers being achievable one day after the interaction for these small fragments. Using photon pressure for collision avoidance does not necessarily require the constellation-based approach initially proposed in this paper for orbit lowering, and could be deployed as an active debris defence system on future high-value stations.

This study did not consider a high fidelity model of the illumination conditions or the presence of the Earth in the field of view, thus these aspects need to be taken into account in the case of a continuous orbit tracking with cameras. Also it was shown that lateral displacements in the ablation case for generic shapes can introduce a further challenge. Further limitations to be considered include the orbital dynamics of the fragments as we did not include all relevant perturbations for a long term evolution of the cloud.

Finally, we investigated the possible spin-up or spin-down of the fragment due to light pressure or ablation and found that, under extreme fluences, there is a tendency for most objects to spin-up, and not to tend towards a stable orientation. The effect was small however, and would not be significant when realistic fluences are considered in the case of photon pressure. In the case of ablation, this spin-up effect is likely to be observed in deployment as the forces involved are much larger than for photon pressure.

Declaration of Competing Interest

The authors declare that they have no known competing financial interests or personal relationships that could have appeared to influence the work reported in this paper.

Acknowledgements

The work in this paper was funded by the University of Strathclyde and Fraunhofer UK Centre for Applied Photonics. The authors would like to thank Dr. Matthew Warden, Dr. John-Mark Hopkins and Simon Andrews from Fraunhofer CAP for their support in this work.

Appendix A. The light reflection model (Eqs. 8, 10 and 11) used in this paper was derived from first principles as below, in order to take into account the degree of 'specularity' of reflections from some materials compared with others, which simpler models (purely specular or purely Lambertian) do not account for. By considering all photons that enter and leave a given surface, we assemble piecewise an expression for the net reaction force considering those photons which are absorbed, reflected specularly, and reflected diffusely. We begin by taking the derivative of the photon energy–momentum relation, considering only a stream of photons entering or leaving a surface.

$$p = \frac{E}{c} \tag{20}$$

$$\frac{dp}{dt} = \frac{P}{c} \tag{21}$$

here p is the photon momentum, E is the photon energy, c is the speed of light and P is the rate of photon energy impinging on or leaving the surface. The rate of change of momentum is of course the definition of force.

A.1. Absorption component

Some portion of the photons incident on a surface will be absorbed, and the rest will be reflected. The parameter which controls this ratio is the reflectivity α, with $\alpha = 1$ indicating 100% reflection, and $\alpha = 0$ indicating 100% absorption. If the light impinging on the surface is from a distant source and can be treated as having parallel rays, it is clear that the direction of the force due to absorption is aligned with the light propagation direction $\hat{\mathbf{i}}$. If the total power of photons impinging on the surface is P_{inc}, then from Eq. 21 the force due to photon absorption is

$$\mathbf{F}_{abs} = \frac{P_{inc}}{c}\hat{\mathbf{i}} \tag{22}$$

A.2. Specular reflection recoil component

The net force due to specular reflection can be calculated similarly. We first introduce a new parameter S, which determines the 'specularity' of a surface - with $S = 1$ being a perfect mirror, and $S = 0$ being a perfect Lambertian surface. We also note that the reflected photons are not aligned with $\hat{\mathbf{i}}$, but propagate in a new direction $\hat{\mathbf{r}}$ according to the law of reflection. Thus the resultant force vector is

aligned with -$\hat{\mathbf{r}}$. Since a fraction αS of the incoming light is reflected specularly, the force due to specular recoil is

$$\mathbf{F}_{spec} = -\alpha S \frac{P_{inc}}{c}\hat{\mathbf{r}} \tag{23}$$

A.3. Diffuse reflection recoil component

The derivation of the Lambertian (diffuse) reflection component is more involved. Lambert's cosine law states that, for rays reflected diffusely at an angle θ to the local normal $\hat{\mathbf{n}}$, their luminous intensity is proportional to the cosine of the angle θ. Since luminous intensity is itself proportional to photon flux/power, this becomes

$$P(\theta) = P_0 \cos\theta \tag{24}$$

where P_0 is the peak power in the direction of the local normal. Integrating this over a hemisphere, one can obtain the expression for the total reflected power

$$P_{diff} = \int_0^{2\pi}\int_0^{\pi/2} P_0 \cos\theta \sin\theta d\theta d\phi \tag{25}$$

$$P_{diff} = \pi P_0 \int_0^{\pi/2} \sin 2\theta d\theta \tag{26}$$

$$P_{diff} = \pi P_0 \tag{27}$$

which of course must be equal to $\alpha(1-S)$. Hence,

$$P_0 = \frac{\alpha(1-S)}{\pi} \tag{28}$$

We must now perform a similar integration to obtain the net reaction force due to Lambertian reflectance. Since we will be integrating over a hemisphere, we need only consider the component of each directional contribution that is aligned with the local normal:

$$\mathbf{F}_{diff} = -\hat{\mathbf{n}}\frac{1}{c}\int_0^{2\pi}\int_0^{\pi} P(\theta)\hat{\mathbf{s}}\cdot\hat{\mathbf{n}}\sin\theta d\theta d\phi \tag{29}$$

where $\hat{\mathbf{s}}$ is the unit vector aligned with the reflected ray, and the additional factor $-\hat{\mathbf{n}}$ indicates the direction of the net reaction force. Since $\hat{\mathbf{s}}\cdot\hat{\mathbf{n}} = \cos\theta$, and substituting Eq. 24:

$$\mathbf{F}_{diff} = -\hat{\mathbf{n}}\frac{2\pi P_0}{c}\int_0^{\pi/2}\cos^2\theta\sin\theta d\theta \tag{30}$$

Recognising that the integral term evaluates to $\frac{1}{3}$, and combining this with Eqs. 28 and 30:

$$\mathbf{F}_{diff} = -\frac{2\alpha(1-S)}{3c}\hat{\mathbf{n}} \tag{31}$$

References

Bhattarai, S., Ziebart, M., Springer, T., et al., 2022. High-precision physics-based radiation force models for the galileo spacecraft. Adv. Space Res. 69 (12), 4141–4154. https://doi.org/10.1016/j.asr.2022.04.003.

CelesTrak (Retrieved 2019). NORAD general perturbations element sets current data. URL: https://celestrak.com/NORAD/elements/.

Chobotov, V.A., 2008. Spacecraft Attitude Dynamics and Control. Krieger Publishing Company; Reprint edition, 15 Dec. 2008.

Di Carlo, M., Graça Marto, S.d., Vasile, M., et al., 2021. Extended analytical formulae for the perturbed keplerian motion under low-thrust acceleration and orbital perturbations. Celestial Mech. Dyn. Astron. 133 (3), 1–39. https://doi.org/10.1007/s10569-021-10007-x.

Gilard, O., Boatella-Polo, C., Dolado-Perez, J.-C., et al., 2010. Corot satellite: analysis of the in-orbit ccd dark current degradation. IEEE Trans. Nucl. Sci. 57 (3), 1644–1653. https://doi.org/10.1109/TNS.2010.2044048.

Jauregui, C., Limpert, J., Tünnermann, A., 2013. High-power fibre lasers. Nat. Photon. 7 (11), 861–867. https://doi.org/10.1038/nphoton.2013.273.

Katz, S., Tal, A., Basri, R., 2007. Direct visibility of point sets. In: ACM SIGGRAPH 2007 papers, pp. 24–es. https://doi.org/10.1145/1276377.1276407.

Mason, J., Stupl, J., Marshall, W., et al., 2011. Orbital debris–debris collision avoidance. Adv. Space Res. 48 (10), 1643–1655. https://doi.org/10.1016/j.asr.2011.08.005.

Pardini, C., Anselmo, L., 2011. Physical properties and long-term evolution of the debris clouds produced by two catastrophic collisions in earth orbit. Adv. Space Res. 48 (3), 557–569. https://doi.org/10.1016/j.asr.2011.04.006.

Phipps, C.R., 2014. L'ADROIT–a spaceborne ultraviolet laser system for space debris clearing. Acta Astronaut. 104 (1), 243–255. https://doi.org/10.1016/j.actaastro.2014.08.007.

Phipps, C.R., Boustie, M., Chevalier, J.-M., et al., 2017. Laser impulse coupling measurements at 400 fs and 80 ps using the luli facility at 1057 nm wavelength. J. Appl. Phys. 122 (19), 193103. https://doi.org/10.1063/1.4997196.

Phipps, C.R., Luke, J.R., Funk, D.J. et al., 2004. Measurements of laser impulse coupling at 130 fs. In: Proceedings SPIE - High-Power Laser Ablation V, vol. 5448, International Society for Optics and Photonics, pp. 1201–1209, https://doi.org/10.1117/12.568419.

Pieters, L., Noomen, R., 2022. Simulating arbitrary interactions between small-scale space debris and a space-based pulsed laser system. Adv. Space Res. https://doi.org/10.1016/j.asr.2022.04.049 (Accepted, in preprint).

SpaceX (Retrieved 2021). Falcon 9 capabilities and services. URL: https://www.spacex.com/vehicles/falcon-9/.

Tran, D., Yogo, A., Nishimura, H., et al., 2017. Impulse and mass removal rate of aluminum target by nanosecond laser ablation in a wide range of ambient pressure. J. Appl. Phys. 122 (23), 233304. https://doi.org/10.1063/1.5005584.

Vasile, M., Maddock, C., Saunders, C., 2010. Orbital debris removal with solar concentrators. In: 61st International Astronautical Congress, 2010 paper IAC-10-A6.4.13.

Walker, L., Vasile, M., 2021. Mitigation of debris in leo using space-based lasers. In: 72nd International Astronautucal Congress paper IAC-21, A6,4,4, x66251.

Walker, L., Vasile, M., Warden, M., 2021. A strategy for mitigation of space debris using space-based continuous-wave laser illumination. In: 8th European Conference on Space Debris. vol. 8.

Wang, B., 2017. Laser ablation impulse generated by irradiating aluminum target with nanosecond laser pulses at normal and oblique incidence. Appl. Phys. Lett. 110 (1), 014101. https://doi.org/10.1063/1.4973464.

Wang, T., 2010. Analysis of debris from the collision of the cosmos 2251 and the iridium 33 satellites. Sci. Global Sec. 18 (2), 87–118. https://doi.org/10.1080/08929882.2010.493078.

Yang, F.Y., Nelson, B., Aziz, J., et al., 2016. LightForce photon-pressure collision avoidance: Efficiency analysis in the current debris environment and long-term simulation perspective. Acta astronautica 126, 411–423. https://doi.org/10.1016/j.actaastro.2016.04.032.

Ziebart, M., Dare, P., 2001. Analytical solar radiation pressure modelling for glonass using a pixel array. J. Geodesy 75, 587–599. https://doi.org/10.1007/s001900000136.